

Nanodevices from and electronic transport properties of ZrI₂ monolayers


Juncai Chen¹, Yongliang Guo², Xiaozheng Fan,¹ Yilian Li,¹ Yi Wu,¹ Chunlan Ma,^{3,*}
Shijing Gong,⁴ Xiao Dong,¹ Tianxing Wang,¹ Guoliang Xu¹, and Yipeng An^{1,†}

¹*School of Physics, Henan Normal University, Xinxiang 453007, China*

²*School of Science, Henan Institute of Technology, Xinxiang 453003, China*

³*School of Physics and Technology, Suzhou University of Science and Technology, Suzhou 215009, China*

⁴*Department of Physics, East China Normal University, Shanghai 200062, China*

 (Received 10 September 2023; revised 16 November 2023; accepted 13 December 2023; published 28 December 2023)

Two-dimensional transition-metal dihalides possess immense potential for applications in low-dimensional nanodevices because of their exceptional thermal and chemical stabilities, unique mechanical and electronic properties, and ultrahigh carrier mobility. In this study, an extensive structural search utilizing first-principles total-energy calculations combined with the particle-swarm optimization algorithm is conducted on bulk ZrI₂ to explore various structures and assess the feasibility of obtaining monolayer phases through mechanical exfoliation. Four stable phases of bulk ZrI₂, namely the $\alpha(\alpha')$ -phase, *hex*-phase, and *tet*-phase, along with their corresponding monolayers, are successfully obtained. All bulk and monolayer phases exhibit dynamic and mechanical stability. The mechanical, electronic transport, and photoelectric properties of the ZrI₂ monolayers are systematically investigated, and conceptual nanodevices based on ml- α - and ml-*hex*-ZrI₂ monolayers are constructed. These nanodevices show remarkable transport characteristics, including excellent rectifying effects, low threshold voltages, high current densities, outstanding field-effect behaviors, and sensitive photoelectric responses. Moreover, *p-n* junction diodes constructed using ml- α -ZrI₂ demonstrate a remarkable negative differential conductance effect. These findings illuminate the multifunctional nature of ZrI₂ monolayers and highlight their potential applications in nanoelectronic devices.

DOI: [10.1103/PhysRevApplied.20.064048](https://doi.org/10.1103/PhysRevApplied.20.064048)

I. INTRODUCTION

Two-dimensional (2D) semiconductors have become popular materials for manufacturing miniaturized and integrated electronic devices because their 2D spatial geometries can significantly reduce the thickness of electronic devices [1]. Additionally, 2D semiconductors exhibit a multitude of unique physical effects owing to the confinement of both charge and heat transport within a single plane, thus holding significant promise for numerous applications across various fields [2–5]. In particular, 2D semiconductors have intrinsic advantages for high-performance microelectronic devices, which can significantly improve device integration and reduce power consumption. In addition, the properties of low-dimensional materials are easier to manipulate according to application requirements. For example, the electronic charge density, magnetism, and superconductivity can be fine tuned with accurately and effectively controlled charge-density wave (CDW) phase

[6–11]. Therefore, they are considered potential successors of silicon materials for extending Moore's law [12].

The main challenge for the widespread use of 2D electronic materials is to find alternatives to Si with high carrier mobility, ambient stability, and a suitable band gap. Many 2D materials, such as phosphorene [13–18], MXenes [19,20], and transition metal dichalcogenides [21–26], have attracted great interest since the discovery of graphene in 2004 [27]. Nevertheless, some 2D materials have inherent shortcomings, such as the zero band gap in graphene [28], low carrier mobility in MoS₂ [29,30], and low chemical stability in α -P [31], significantly limiting their practical applications. Recently, 2D metal halides have attracted great interest because of their extraordinary properties, such as suitable band gaps, high carrier mobility, and high stability [32]. For instance, layered BiI₃ has been successfully synthesized [33], and has demonstrated room-temperature band-edge photoluminescence with a band gap of 1.8 eV for the bulk [33] and 1.57 eV for the monolayer [34]. A magnetic semiconducting NiI₂ monolayer was prepared [35] using the vapor deposition method and was proven to exhibit good semiconducting transport behavior, spin-filtering effects, and

*wxmcl@mail.usts.edu.cn

†ypan@htu.edu.cn

photoelectric properties, making it suitable as a potential material for spintronic and optoelectronic devices [35,36]. The group 11 transition metal halide CuBr, CuI, AgBr, and AgI monolayers, with a direct band gap of approximately 3.12–3.36 eV and high carrier mobility (approximately $10^3 \text{ cm}^2 \text{ V}^{-1} \text{ s}^{-1}$), exhibit high thermodynamic, dynamic and mechanic stabilities, demonstrating great potential for photocatalysis and quantum cutting [37]. Theoretical calculations demonstrated a stable PbI_2 monolayer exhibiting Frenkel-like Wannier-Mott exciton and spin-orbit coupling effects [38,39]. The large-scale PbI_2 monolayers and few layers were synthesized [40] via a facile physical vapor deposition method.

In particular, 2D zirconium dihalides, ZrX_2 ($X = \text{Cl}, \text{Br}, \text{I}$), have attracted considerable attention because of their unique mechanical, electronic, and multiferroic properties. The van der Waals (vdW) system of the ZrI_2 bilayer was reported to possess ferroelastic-ferroelectric multiferroics resulting from interlayer sliding [41–43]. Very recently, light-matter interactions, such as photo-magnetization [44] and photogalvanic [45] effects of the ZrI_2 bilayer by interlayer sliding, have been investigated. Furthermore, ZrI_2 monolayers exhibit excellent thermoelectric performance, i.e., the largest merit (ZT) value of the $P2_1/m$ phase is 7.86 at 700 K [46], and the ZT value of the n -type (electron doping) 2H- ZrI_2 phase is 3.57 at 900 K [47]. In addition, the valley spin-splitting behavior of the 2H- ZrI_2 monolayer was investigated and proposed as a promising 2D valleytronics material [48]. Notably, Zhang *et al.* [49] reported hexagonal ZrI_2 monolayer to exhibit very high carrier mobility ($5138 \text{ cm}^2 \text{ V}^{-1} \text{ s}^{-1}$ for the hole). This mobility is the second highest among monolayer semiconductors, significantly surpassing the mobility of bulk silicon ($1400 \text{ cm}^2 \text{ V}^{-1} \text{ s}^{-1}$). Therefore, 2D zirconium dihalides are excellent candidates for the development of optoelectronic, ferroelectric, thermoelectric, and valleytronic applications and related nanodevices. In fact, such materials attracted attention as early as the 1980s. For example, two polymorph forms of layered bulk ZrI_2 , namely the α -phase (space group $P2_1/m$) and β -phase (space group $Pmn2_1$), were synthesized experimentally and found to coexist [50,51]. In 2021, Ding *et al.* [42] clarified the phase competition relationship between the parent phase s - ZrI_2 , and the derived phases nonpolar α - ZrI_2 and polar β - ZrI_2 . Few-layered or monolayered ZrI_2 can be obtained from layered bulk structures via mechanical exfoliation. It is feasible for the mechanical exfoliation of bilayer ZrI_2 from the bulk structure as the cleavage energy is estimated to be 0.28 J m^{-2} [41], which is smaller than that of graphene (0.37 J m^{-2}) [52]. However, whether $P2_1/m$ and 2H-phase ZrI_2 monolayers can be easily obtained via mechanical exfoliation has not yet been investigated. Moreover, although the hexagonal phase of ZrI_2 monolayer has been reported in the Computational 2D Materials Database [53] and its thermoelectrics,

valleytronics, and carrier mobility are investigated by various research groups [47–49], the existence of its parent bulk phase has never been reported. In addition, detailed studies of the mechanical properties, transport behaviors, field-effect behaviors, and photoresponse characteristics of the various phases of the ZrI_2 monolayer, useful for a fundamental understanding of the underlying mechanisms in device architectures, are limited.

In this study, we performed an extensive structural search for bulk ZrI_2 using first-principles total-energy calculations combined with the particle-swarm optimization (PSO) algorithm [54] to identify the parent structures of monolayer phases and determine the feasibility of obtaining monolayer phases by mechanical exfoliation. Furthermore, the dynamic and mechanical stabilities of both the bulk and monolayer phases were identified. Then, the electronic properties of the ZrI_2 monolayer and the transport properties of some conceptual nanodevices, such as p - n junction diodes, field-effect transistors (FETs), and phototransistors, are investigated within the density-functional-theory (DFT) framework combined with the nonequilibrium Green's function (NEGF) [55] method.

II. CALCULATION METHODS

In this study, the experimental simulations were divided into two parts. The first part involved structural prediction, crystal stability verification, and mechanical property calculations. The second part was electronic property and transport behavior calculations.

The first part calculations were performed using the Vienna *ab initio* simulation package (VASP) [56,57] with the projector augmented-wave scheme (PAW) [58,59]. The Kohn-Sham equations were solved using the exchange-correlation functional following the generalized gradient approximation (GGA) of Perdew-Burke-Ernzerhof (PBE) [60] with a kinetic energy cutoff of 600 eV. The total energy convergence threshold was set to 10^{-6} eV in the electronic self-consistent loop. The structural prediction was conducted by combining first-principles total energy calculations with the PSO algorithm [54] as implemented in the CALYPSO code [61], which has been proven effective and accurate in predicting the crystal structures of a large variety of materials [62–68]. This approach requires only chemical compositions for a given compound to predict stable or metastable structures at given external conditions [54]. The PSO algorithm, which is an unbiased global optimization method, is best known for its ability to conquer large barriers of energy landscapes by making use of the swarm intelligence and by self-improving structures. In the structural prediction, the search space was performed with system sizes ranging from 1 to 8 formula units (f.u.) of ZrI_2 per simulation cell. The total number of structures per generation was set as 30, and the PsoRatio is set as 0.6.

Namely, the software generates randomly the first generation of 30 structures according to the given element ratio, and optimizes these structures with VASP code. Starting from the second generation, 60% of the structure of each generation was generated based on the previous generation structures, and the rest of the structures, whose symmetries must be distinguished from any of the previously generated ones, will then be generated randomly. Finally, all the predicted structures were ranked in enthalpy order to select the energetically best structures. For the multilayer configurations, a damped vdW correction (DFT-D3) [69,70] was adopted to accurately describe the interlayer interaction. In the 2D monolayer systems, the periodic slabs were separated by a vacuum spacing of approximately 30 Å to avoid interactions between adjacent layers. To investigate the thermal stability, the *ab initio* molecular dynamics (AIMD) simulations were performed using the Nosé-Hoover thermostat scheme in the NVT ensemble at 300 K with the total simulation time of 10 ps and a time step of 1 fs by using the VASP code.

The second part calculations were performed using the QuantumATK code [71] with linear combinations of atomic orbitals (LCAO) basis sets, using a PBE functional to solve the exchange-correlation interactions. The accuracy of LCAO basis sets depends on the number of orbitals and the range of the orbitals. Increasing the number of orbitals and their range decreases the efficiency and increases the memory requirement. In this study, the norm-conserving PseudoDojo pseudopotentials [72] were employed to describe the core electrons. Three different basis sets are available for each element when using the PseudoDojo pseudopotentials: medium, high, and ultra. The medium basis set is default for the PseudoDojo pseudopotentials, and should be sufficient for most applications. To obtain more accurate results, the high basis set for the PseudoDojo pseudopotentials was selected in this study, and the visualizing of this basis set for the Zr and I atoms was shown in Figs. S1(a) and S1(b) within the Supplemental Material [75]. In addition, the electronic band structures of the ml-*hex*-phase of ZrI₂ have been calculated by using the PAW and LCAO within the VASP and QuantumATK code at similar calculation level, respectively, as shown in Fig. S1(c) within the Supplemental Material [75]. It can be seen that the electronic band structures calculated by the two methods agree well with each other, indicating that it can obtain reliable results using LCAO basis sets in the simulation. A real-space grid density mesh cutoff of 80 hartree was used. To simulate the device systems, the NEGF formalism is implemented in combination with DFT-LCAO. Detailed of the device models and simulation methods can be found in our previous study [73]. The Brillouin zone (BZ) of the device electrodes was sampled using a $10 \times 1 \times 200$ k -point mesh generated via the Monkhorst-Pack scheme [74]. The residual force on each atom convergence criterion was set to $0.001 \text{ eV \AA}^{-1}$,

and the total energy-convergence threshold was set to 10^{-6} eV .

III. RESULTS AND DISCUSSION

A. Crystal structure and electronic properties

Bulk monoclinic α -ZrI₂ was synthesized by Guthrie *et al.* [50] and was identified as a phase with an isostructure with WTe₂ (space group $P2_1/m$), as shown in Fig. 1(a). The orthorhombic β -ZrI₂ phase, which is isostructural with WTe₂ (space group $Pmn2_1$), exhibits coherent intergrowth with α -ZrI₂. Corbett *et al.* [51] synthesized β -ZrI₂ and its structural information was thoroughly analyzed. Furthermore, we performed a structural search for the bulk ZrI₂ system using first-principles total-energy calculations and the PSO algorithm [54] to explore possible alternative structures. Remarkably, this procedure successfully reproduced the monoclinic α -ZrI₂ phase ($P2_1/m$) synthesized in the experiment, as shown in Fig. 1(a). The structure search also identified three other structures: a hexagonal structure, a tetragonal structure, and a monoclinic structure with the space groups $P6_3/mmc$, $I4/mmm$, and $C2/m$, as shown in Figs. 1(b), 1(c) and S2 within the Supplemental Material [75], respectively. The hexagonal $P6_3/mmc$ phase (denoted as *hex*-phase) contains two ZrI₂ f.u. per unit cell. In this phase the Zr atoms occupy the $2d$ Wyckoff positions (1/3, 1/3, 0.75) and the I atoms occupy the $4f$ Wyckoff positions (1/3, 1/3, 0.118). The tetragonal $I4/mmm$ phase (denoted as *tet*-phase) contains two ZrI₂ f.u. per unit cell. Here, the Zr atoms occupy the $2b$ Wyckoff positions (0, 0, 0.5) and the I atoms occupy the $4e$ Wyckoff positions (0, 0, 0.872). Similarly, the monoclinic $C2/m$ phase (denoted as α' -phase) contains four ZrI₂ f.u. per unit cell. In this phase, the Zr atoms occupy the $4i$ Wyckoff positions (0.5, 0.693, 0.754), whereas the I atoms occupy the $4i$ Wyckoff positions (0.5, 0.876, 0.140) and (0, 0.640, 0.894). In Table I, the calculated lattice constants for the ZrI₂ phases are listed and compared with the available experimental data for the α -ZrI₂ phase. The calculated results agree well with the experimental data. Comparing the previously reported and our calculated results shows that all three phases (α , β , and α') of ZrI₂ exhibit layered structures consisting of buckled I-Zr-I trilayers, connected by weak van der Waals interactions. Additionally, I-Zr-I layers of the three phases exhibit the same structure, where zigzag chains of zirconium atoms are situated between essentially double hexagonal close-packed layers of iodine [51]. The layers of α - and β -phases are stacked identically, and the transition between the two phases can be realized through an interlayer slip. Unlike the first two, the interval layers of α' phase are rotated 180° in plane compared with the α -phase, as depicted in the sketch map shown in Fig. S2 within the Supplemental Material [75]. To determine the mechanical and dynamic stabilities, we calculated the phonon dispersion curves (Fig. S3 within

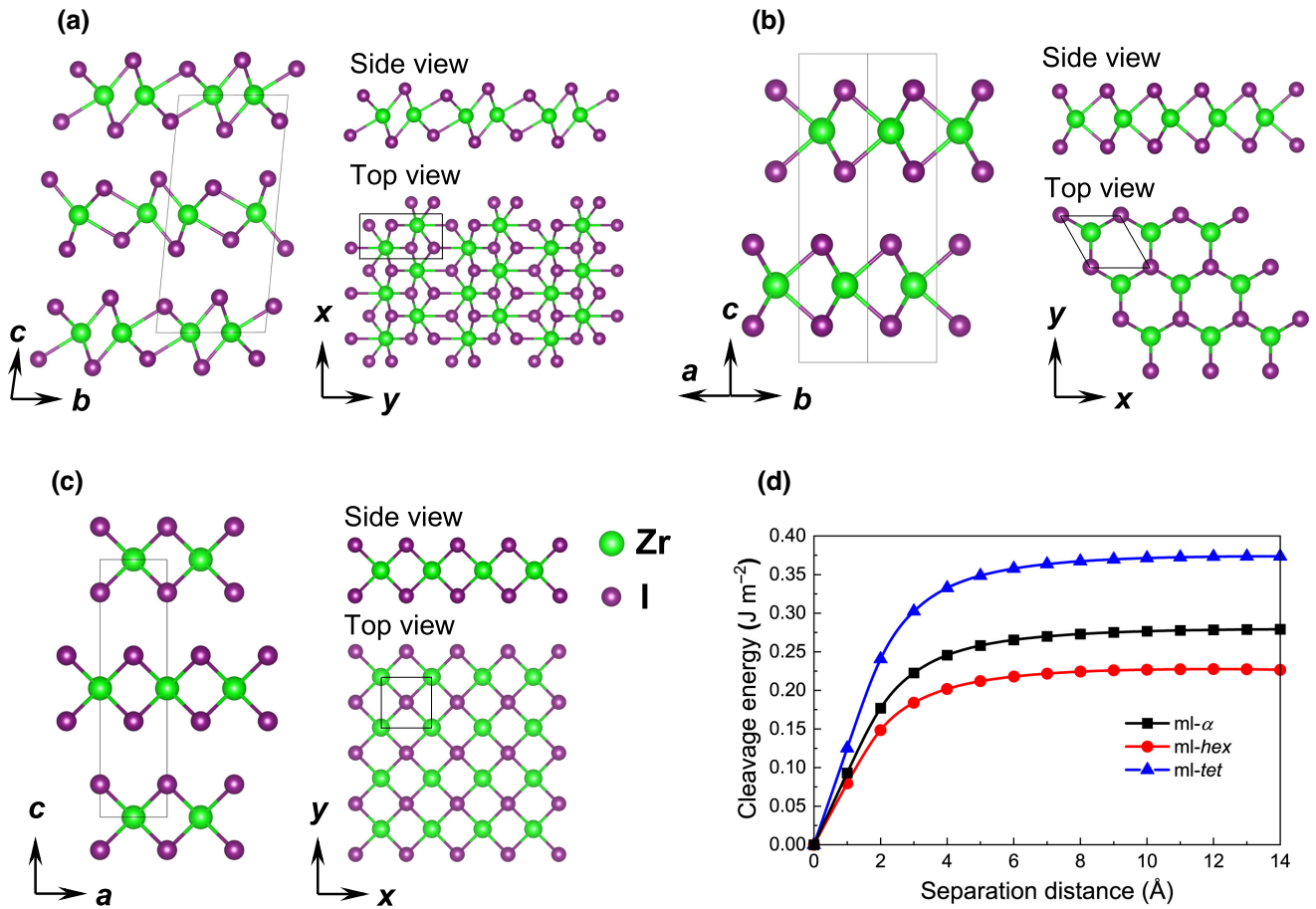


FIG. 1. Crystal structures and cleavage energy. Bulk structures of ZrI₂ and side and top view of monolayer structures exfoliated from the corresponding bulk structure for (a) α -phase, (b) hex -phase, and (c) tet -phase. (d) Cleavage energy versus the separation distance between ZrI₂ monolayer and six layer for the α -, hex -, and tet -phases.

the Supplemental Material [75]) and elastic constants C_{ij} (Table S1 within the Supplemental Material [75]). None of the phonon dispersion curves have imaginary modes in the Brillouin zone, and the elastic constants C_{ij} satisfy the Born-Huang mechanical stability criteria [77,78], confirming the dynamic and mechanical stabilities. To

study the relative energetic stability of the various phases of bulk ZrI₂, we have calculated the total energy versus volume, as shown in Fig. S4(a) within the Supplemental Material [75]. Both total energies and volumes of the α -phase and α' -phase are very close to each other, this is because the atomic configurations of these two phases are

TABLE I. Lattice constants of the bulk and monolayer phases of ZrI₂.

	System	a (Å)	b (Å)	c (Å)	β (°)
Bulk	α -phase	3.746	6.853	14.981	95.69
		3.741 [50]	6.821 [50]	14.937 [50]	95.66 [50]
		3.749 [42]	6.865 [42]	14.881 [42]	95.95 [42]
	hex -phase	3.799	3.799	14.726	
	tet -phase	3.559	3.559	13.711	
Monolayer	α' -phase	3.776	6.843	15.222	100.48
		3.764	6.905		
		3.76 [76]	6.91 [76]		
	$ml-hex$ -phase	3.67 [46]	6.75 [46]		
		3.823	3.823		
		3.80 [48]	3.80 [48]		
		3.585	3.585		

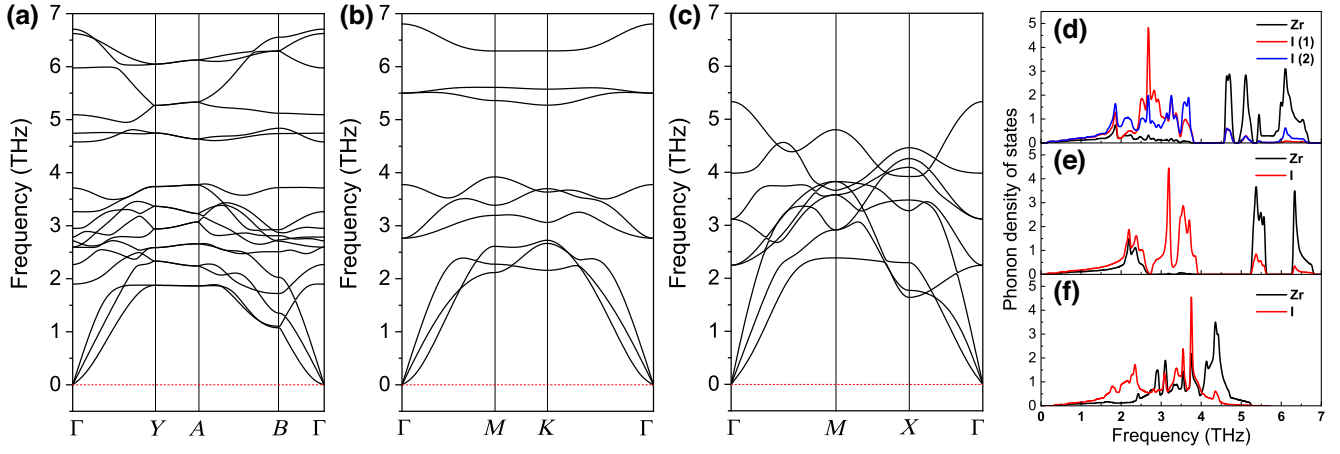


FIG. 2. Phonon dispersion curves for (a) ml- α -phase, (b) ml-hex-phase, and (c) ml-tet-phase of ZrI₂ monolayer and their corresponding element-projected phonon density of states (d)–(f), respectively. I(1) and I(2) in (d) represent the I atom in the nonequivalent position in the ml- α -phase.

very similar. And these two phases are energetically the most favorable among the phases of ZrI₂. Nevertheless, the energy of the *tet*-phase is the highest, as well as the volume of this phase is the smallest among the phases of ZrI₂. To further investigate the thermostability, the Helmholtz free energy $F(V, T)$ was calculated considering the vibrational energy of the lattice ions, as the following formula:

$$F(V, T) = E(V) + F_{\text{vib}}(V, T), \quad (1)$$

where $E(V)$ is the ground-state total energy, $F_{\text{vib}}(V, T)$ is the vibrational energy of the lattice ions, which is determined by

$$F_{\text{vib}}(V, T) = k_B T \int_0^\infty g(\omega) \ln \left[2 \sinh \left(\frac{\hbar \omega}{2k_B T} \right) \right] d\omega, \quad (2)$$

where $g(\omega)$ is the phonon density of states (PDOS). In addition, this formula is not suitable for dynamically unstable systems because it strictly requires that all the phonon frequencies ω are positive. The Helmholtz free energies $F(V, T)$ of the bulk and monolayer phases of ZrI₂ for the temperature range from 0 to 1000 K are shown in Figs. S4(b) and S4(c) within the Supplemental Material

[75], respectively. The results indicate that the monoclinic structures of the bulk and monolayer ZrI₂ are the thermodynamically most stable phase. Meanwhile, all the phases do not undergo temperature-induced phase transitions, because the curves of the Helmholtz free energies of the phases do not intersect throughout the range of 0–1000 K.

Owing to the weak van der Waals interactions between the layers of bulk ZrI₂, the monolayer of ZrI₂ can be easily exfoliated from the bulk structures. The monolayers of ZrI₂ exfoliated from the bulk $P2_1/m$, $P6_3/mmc$, and $I4/mmm$ structures are shown on the right side of Figs. 1(a)–1(c), respectively, and the corresponding ZrI₂ monolayers are denoted as ml- α -phase ($P2_1/m$), ml-hex-phase ($P\bar{6}m2$) and ml-tet-phase ($P4/mmm$). To evaluate the feasibility of obtaining the ml- α -phase, ml-hex-phase, and ml-tet-phase through mechanical exfoliation from the bulk phase, we calculated their respective cleavage energies, as shown in Fig. 1(d). The cleavage energies of the ZrI₂ monolayer separated from the bulk $P2_1/m$, $P6_3/mmc$, and $I4/mmm$ phases were estimated as 0.28, 0.23, and 0.37 J m⁻², respectively. The cleavage energy of the ml-tet-phase is comparable to the experimentally estimated value of graphene (0.37 J m⁻²) [52], and the ml- α -phase and

TABLE II. Calculated in-plane elastic stiffness constants C_{ij} , Young's modulus $E(\theta)$, shear modulus $G(\theta)$, in units of N m⁻¹, and Poisson's ratio $\nu(\theta)$ for the phases of the ZrI₂ monolayer.

System	Elastic stiffness constant				$E(\theta)$		$G(\theta)$		$\nu(\theta)$	
	C_{11}	C_{22}	C_{66}	C_{12}	max	min	max	min	max	min
ml- α -phase	77.7	77.3	28.0	18.1	73.4	70.6	29.7	28.0	0.261	0.233
ml-hex-phase	75.6		29.0	17.6	71.4	71.4	29.0	29.0	0.233	0.233
ml-tet-phase	109.7		33.0	14.0	108.0	86.0	47.9	33.0	0.305	0.128
graphene	357.7		145.0	67.6	344.8	344.8	145.0	145.0	0.189	0.189
graphene [80]	349.1		144.4	60.3	338.7	338.7	144.4	144.4	0.173	0.173

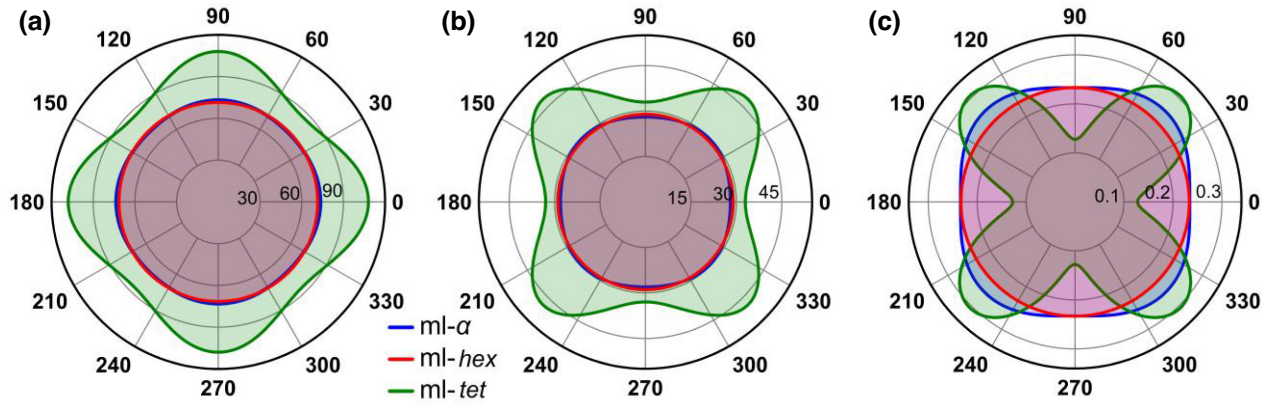


FIG. 3. Calculated orientation-dependent (a) Young's modulus $E(\theta)$, (b) shear modulus $G(\theta)$, and (c) Poisson's ratio $\nu(\theta)$ for monolayer ZrI_2 . The $E(\theta)$ and $G(\theta)$ are in units of $N m^{-1}$, and the angles are in degree units.

ml-hex-phase are mechanically exfoliated more easily than the *ml-tet*-phase and graphene. To investigate the dynamic stability of the ZrI_2 monolayers, their phonon dispersion curves were calculated, as shown in Figs. 2(a)–2(c). None of the phonon dispersion curves of the three ZrI_2 monolayers exhibit imaginary modes in the Brillouin zone, indicating that the monolayers are dynamically stable. In addition, the element-projected PDOS of various ZrI_2 monolayers were shown in Figs. 2(d)–2(f). From the phonon dispersion curves and PDOS in Fig. 2, it can be seen that *ml- α* -phase and *ml-hex*-phase ZrI_2 monolayers have optical branches with higher frequencies (approximately 5–7 THz), while *ml-tet*-phase does not. This results in a band gap between the high-frequency branches (approximately 5–7 THz) and the low-frequency branches (approximately 0–4 THz) of the *ml- α* -phase and *ml-hex*-phase. The PDOS shows that the optical branches of higher oscillating frequencies are mainly from the contribution of Zr atoms. For all the three phases of ZrI_2 monolayers, the acoustic and relatively low-frequency optical branches come from co-contributions with Zr and I atoms, and the vibrational coupling between Zr and I is strong in this frequency region (approximately 0–4 THz). These phenomena are mainly due to the fact that the mass of the I atom is greater than the Zr atom; and the chemical bond strength of *ml-tet*-phase is more uniform than *ml- α* -phase and *ml-hex*-phase. For example, it can be seen that there is a relatively strong “dimer bond” between Zr-Zr in *ml- α* -phase from the crystal structure in Fig. 1(a).

By using AIMD simulations, the thermal stabilities of the various phases of ZrI_2 monolayers are examined at room temperature (300 K). The AIMD simulations are carried out with a $6 \times 3 \times 1$, $6 \times 6 \times 1$, and $6 \times 6 \times 1$ supercells for *ml- α* -phase, *ml-hex*-phase, and *ml-tet*-phase, respectively. Our calculations demonstrate that the atomic structures of the ZrI_2 monolayers are still robust after 10 ps of heating as shown in Figs. S5(a)–S5(c) within the Supplemental Material [75]. There is no structural transition and remarkable distortions, as well as no bond

breaking in these ZrI_2 monolayers. Their total energies only fluctuate around a certain constant magnitude for AIMD running, indicating their thermal stabilities at room temperature.

Furthermore, the elastic constants C_{ij} of the monolayer phases were obtained using the stress-strain method [79] to determine their mechanical stability, as listed in Table II. The number of independent elastic constants is associated with the symmetry of the 2D crystal. The *ml- α* -phase is a monoclinic structure in which the independent elastic constants reduce to four components, C_{11} , C_{22} , C_{66} , and C_{12} , and the corresponding mechanical stability criteria are given as [77,80] $C_{11} > 0$, $C_{66} > 0$, and $C_{11}C_{22} > C_{12}^2$. The *ml-hex*-phase has a hexagonal structure with two independent elastic constants, C_{11} and C_{12} , and $C_{66} = (C_{11} - C_{12})/2$. The corresponding mechanical stability criteria are [77,80] $C_{11} > 0$ and $C_{11} > |C_{12}|$. The *ml-tet*-phase has a tetragonal structure, in which the independent elastic constants reduce to three components: C_{11} , C_{66} , and C_{12} . The corresponding mechanical stability criteria are given as [77,80] $C_{11} > 0$, $C_{66} > 0$, and $C_{11} > |C_{12}|$. According to the elastic constants C_{ij} listed in Table II, all three phases satisfied their respective mechanical stability criteria, confirming their mechanical stability.

Next, we further investigated the mechanical properties and elastic anisotropies of ZrI_2 monolayers. The orientation-dependence of Young's modulus $E(\theta)$, shear modulus $G(\theta)$, and Poisson's ratio $\nu(\theta)$ were calculated using the following equations [81,82]:

$$1/E(\theta) = S_{11}c^4 + S_{22}s^4 + S_{16}c^3s + S_{26}cs^3 + (S_{66} + 2S_{12})c^2s^2 \quad (3)$$

$$\nu(\theta)/E(\theta) = (S_{66} - S_{11} - S_{22})c^2s^2 - S_{12}(c^4 + s^4) + (S_{26} - S_{16})(cs^3 + c^3s) \quad (4)$$

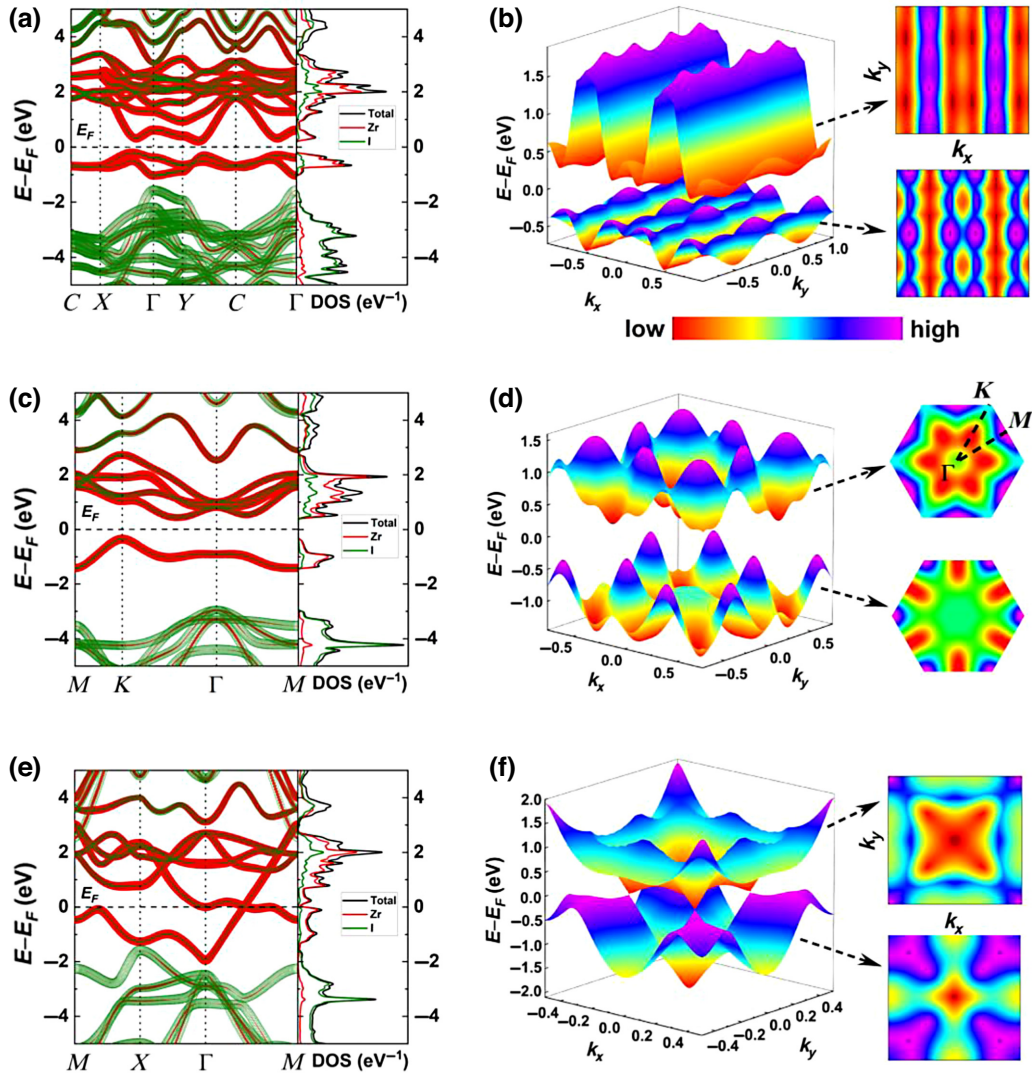


FIG. 4. Element-projected electronic band and density of states for the (a) ml- α -phase, (c) ml-hex-phase, and (e) ml-tet-phase phases of the ZrI₂ monolayer. The red and green lines are the projection of Zr and I atoms. 3D views of the top of the conduction band and bottom of the valence band, and 2D projections in the Brillouin zone for the corresponding (b) ml- α -phase, (d) ml-hex-phase, and (f) ml-tet-phase.

and

$$\begin{aligned} 1/4G(\theta) = & (S_{11} + S_{22} - 2S_{12})c^2s^2 + S_{66}(c^2 - s^2)^2/4 \\ & - (S_{16} - S_{26})(c^3s - cs^3) \end{aligned} \quad (5)$$

where $s = \sin(\theta)$, $c = \cos(\theta)$, $\theta \in [0, 2\pi]$ is the angle with respect to the $+x$ axis, and $S_{ij} = C_{ij}^{-1}$ are second-order elastic compliance constants. Our obtained orientation-dependence elastic moduli are shown in Fig. 3. Meanwhile, the minimum and maximum values of Young's modulus $E(\theta)$, shear modulus $G(\theta)$, and Poisson's ratio $\nu(\theta)$ for these systems are listed in Table II. For comparison purpose, the results of the graphene including our calculated and previous reported [80] values are also shown in Table II. The $E(\theta)_{\max}$ and $G(\theta)_{\max}$ values of the

ml- α -phase and ml-hex-phase are lower than that of ml-tet-phase. It is found that the difference between the minimum and maximum values of $E(\theta)$, $G(\theta)$, and $\nu(\theta)$ for the ml- α -phase of the ZrI₂ monolayer is very small, and those for ml-hex-phase equal zero, nevertheless, those for ml-tet-phase are considerable larger than that of the first two phases. The results demonstrate that the ml- α -phase has a weak elastic anisotropy, while the ml-hex-phase and ml-tet-phase show an elastic isotropy and a strong elastic anisotropy, respectively. Note that the $E(\theta)_{\max}$ and $G(\theta)_{\max}$ values of all the ZrI₂ monolayers are smaller than those of graphene ($E(\theta)_{\max} = 339 \text{ N m}^{-1}$, $G(\theta)_{\max} = 144 \text{ N m}^{-1}$) [80] and BN monolayer ($E(\theta)_{\max} = 227 \text{ N m}^{-1}$, $G(\theta)_{\max} = 114 \text{ N m}^{-1}$) [80]. However, they are comparable with that of BP monolayer ($E(\theta)_{\max} = 92 \text{ N m}^{-1}$, $G(\theta)_{\max} = 28 \text{ N m}^{-1}$)

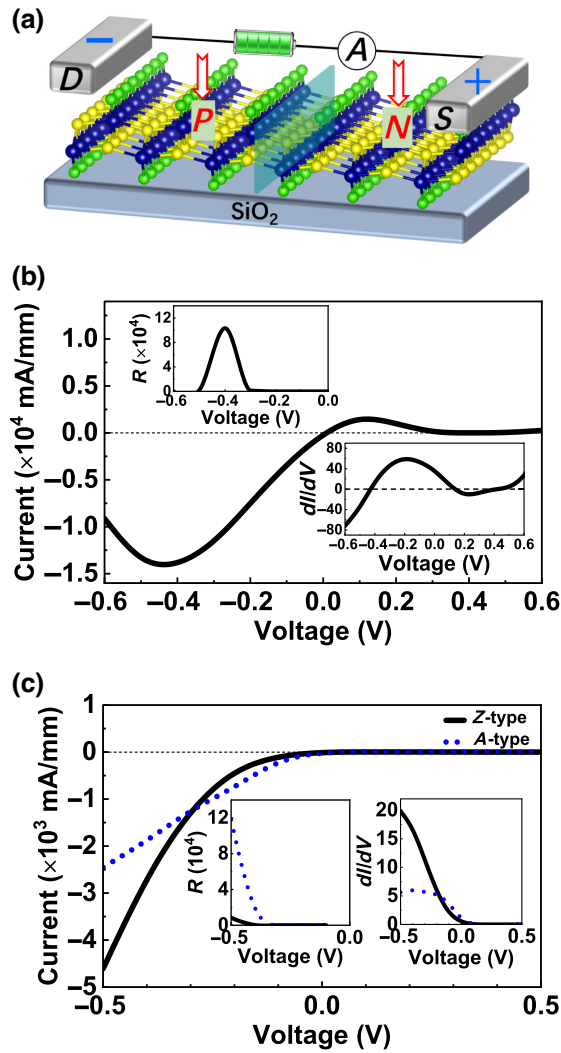


FIG. 5. (a) Schematic of the p - n junction diode of the ZrI_2 monolayer. Bias-dependent current of the p - n junction diode, with rectification ratio and difference conductance curves shown in the inset for (b) $\text{ml-}\alpha$ -phase and (c) ml-hex -phase.

[80] and MoS_2 monolayer ($E(\theta)_{\max}=122 \text{ N m}^{-1}$, $G(\theta)_{\max}=49 \text{ N m}^{-1}$) [80]. These indicate that the mechanical strength of ZrI_2 monolayers is similar to BP and MoS_2 , but weaker than graphene and BN.

To investigate the electronic properties of the monolayer phases of ZrI_2 , the atom-resolved electronic band structures, the density of states (DOS), and 3D views and 2D projections of the top of the valence band (TVB) and the bottom of the conduction band (BCB) were calculated, as shown in Fig. 4. The band structures indicate that both the $\text{ml-}\alpha$ -phase and ml-hex -phase are indirect band gap semiconductors, whereas the ml-tet -phase is a metal. The band gap of the $\text{ml-}\alpha$ -phase is 0.430 eV, and the valence band maximum (VBM) is located between the Z and Γ points; the conduction band minimum (CBM) is located between the Y and C points, as shown in Fig. 4(a). The band gap

of the ml-hex -phase is 0.787 eV, and the VBM is located at the K point; the CBM is located between the K and Γ points, as shown in Fig. 4(c), which is in good agreement with previously reported results ($E_g = 0.77 \text{ eV}$ [48] and 0.687 eV [49]). The element-projected electronic band and density of states in Figs. 4(a), 4(c), and 4(e) show that the bands around the Fermi level for the three ZrI_2 monolayers were predominantly attributed to the orbitals of the Zr atoms.

The electronic structure near the Fermi level was analyzed in detail using 3D views of the TVB and BCB, and their 2D projections. As shown in Fig. 4(b), both the TVB and BCB of the $\text{ml-}\alpha$ -phase were wavy in the k_x direction. The carrier effective masses m^* for the electrons (holes) were 0.365 (1.052) and 1.708 (0.784) m_e along the x and y directions at 300 K, respectively. Our results are consistent with those of Jia *et al.* [46], who reported a maximum carrier mobility of up to $2289.61 \text{ cm}^2 \text{ V}^{-1} \text{ S}^{-1}$ (hole) [46]. Zhang *et al.* [49] reported a carrier mobility of up to approximately $5000 \text{ cm}^2 \text{ V}^{-1} \text{ S}^{-1}$ (hole) for the ml-hex -phase of the ZrI_2 monolayer, which is one of the first two highest mobility 2D semiconductors (BSb and ZrI_2 monolayer). The electronic band around the Fermi level partly explains the very high mobility of the ml-hex -phase of the ZrI_2 monolayer. Figure 4(d) shows that funnel-shaped bands were formed at the VBM and CBM. The carrier effective masses m^* for electrons (holes) were 1.103 (0.379) and 0.571 (0.376) m_e along the x and y directions at 300 K, respectively, which agrees with the Drude effective mass (approximately $0.40 m_e$) reported by Zhang *et al.* [49] and is comparable to that of MoS_2 ($0.43 m_e$). The ml-tet -phase of the ZrI_2 monolayer has a conelike band structure near the Fermi level to that of graphene, as shown in Fig. 4(f). If the band gap can be opened through some approaches, it may greatly increase its application prospects. The high carrier mobility of the $\text{ml-}\alpha$ -phase and ml-hex -phase 2D semiconductors at room temperature makes them promising candidates for next-generation electronics and optoelectronics. Therefore, we explore the transport properties of some conceptual devices, including p - n junction diodes, FETs, and phototransistors, constructed using the $\text{ml-}\alpha$ -phase and ml-hex -phase of the ZrI_2 monolayer in the following sections.

B. Transport properties of ZrI_2 monolayer p - n junction diodes

ZrI_2 monolayers are expected to exhibit good transport behavior because of their high carrier mobility [46, 49]. Therefore, p - n junction diodes with $\text{ml-}\alpha$ -phase and ml-hex -phase ZrI_2 monolayers serving as the transmission medium are constructed using an electrostatic doping method with p - and n -type atom-compensation charges [83]. The schematic of the p - n junction diode is shown in Fig. 5(a). The diode contains a drain electrode (D), a source

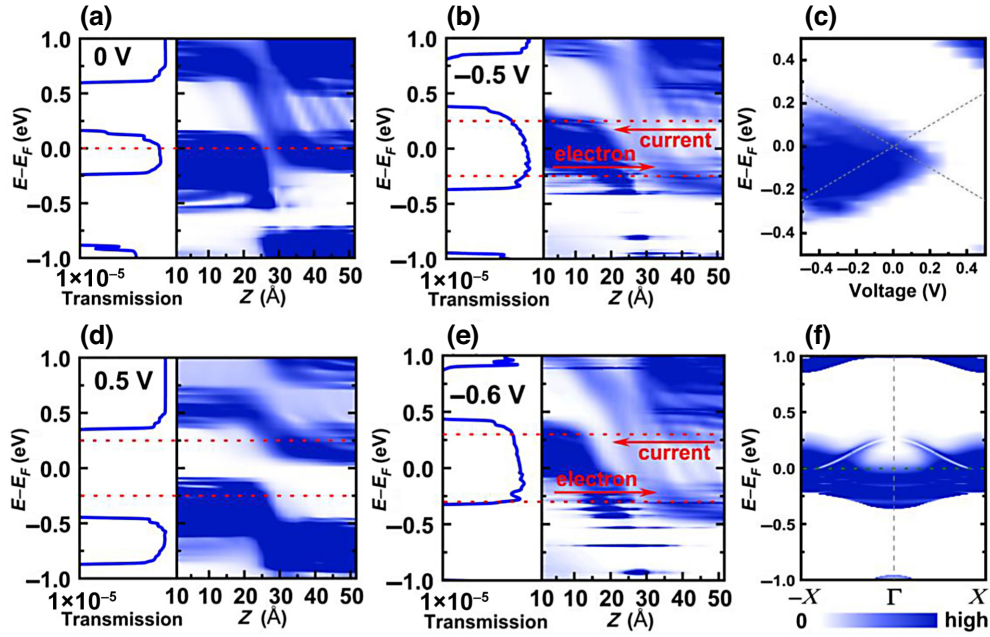


FIG. 6. Transmission coefficient $T(E)$, projected local density of states (PLDOS) under biases of 0 V (a), -0.5 V (b), and 0.5 V (d), -0.6 V (e), and (c) transmission spectra $T(E, V)$ and (f) k -dependent transmission coefficients $T(E, k)$ at -0.5 V for the p - n junction diode of ml - α -phase ZrI_2 . The red dashed lines in (a), (b), (d), and (e), and the crossing, gray dashed lines in (c) are bias window. The color map shows data from 0 (white) to high (blue).

electrode (S), and a central scattering region (p - n junction). In this study, the D and S electrodes are constructed using periodic p - and n -doped ZrI_2 monolayer, respectively. The current through the p - n junction diode when a D - S bias of V_b is applied is calculated as [84]

$$I(V_b) = \frac{2e}{h} \int_{-\infty}^{\infty} T(E, V_b) [f_D(E - \mu_D) - f_S(E - \mu_S)] dE, \quad (6)$$

where e is the electron charge, and h is Planck's constant. $T(E, V_b)$ is the transmission coefficient. The Fermi-Dirac distribution function of the D (S) electrode is expressed as $f_{D(S)} = \{1 + \exp[E - \mu_{D(S)}/k_B T_{D(S)}]\}^{-1}$, and $\mu_{D(S)}$ and $T_{D(S)}$ are the corresponding chemical potential and temperature. To accurately describe electron behavior at finite temperature, the Fermi-Dirac distribution-function broadening is typically set between 0.01 and 0.1 eV. In this study, we adopt the default value of 0.026 eV in QuantumATK, corresponding to a temperature of 300 K. The calculated I - V curves of the ml - α -phase and ml - hex -phase ZrI_2 monolayers with a doping concentration of $2.5 \times 10^{14} \text{ cm}^{-2}$ for p - and n -type carriers are shown in Figs. 5(b) and 5(c). In the p - n junction diode of the ml - α -phase, the x -direction of the lattice [see Fig. 1(a)] represents the transmission direction. The I - V curve in Fig. 5(b) shows that a current is generated when a forward or reverse bias voltage is applied. The current reaches its maximum at 0.1 V on the positive and 0.4 V on the negative bias sides. Subsequently, the current

decreases when the applied bias exceeds the two critical points on the positive and negative bias sides. Therefore, the I - V curve shows a strong negative differential conductance (NDC) in a bias range of 0.1 to 0.4 V and -0.4 to -0.6 V [see dI/dV versus voltage shown in the inset at the lower right of Fig. 5(b)]. The rectification ratio (R), which describes the unidirectional transport features of a diode, is given as $R = |I(-V_b)/I(V_b)|$. The maximum magnitude of R for the p - n junction diode of the ml - α -phase is 10^5 at a bias of -0.4 V, as shown in Fig. 5(b). However, the R is relatively small beyond a bias range of -0.3 to -0.5 V, indicating that the unidirectional transport performance of this p - n junction diode is not very impressive.

To further investigate the transport properties, we calculated the projected local density of states (PLDOS), transmission coefficients $T(E)$, transmission spectra $T(E, V)$, and k -dependent transmission coefficients $T(E, k)$ for the p - n junction diode of the ml - α -phase, as shown in Fig. 6. The PLDOS in Fig. 6(a) shows that the bands of the p - and n -doped terminals overlap near the Fermi level, although the ml - α -phase is a semiconductor. This behavior is attributed to the doping used for constructing the p - n junction. As a result, a small bias voltage can induce current flow in both forward and reverse directions. Moreover, the PLDOSs in Figs. 6(a), 6(b) and 6(d) indicate that applying a positive bias on the p - n junction causes the bands of the p - and n -doped terminals to shift up and down accordingly, and vice versa. The current density reaches a maximum of approximately

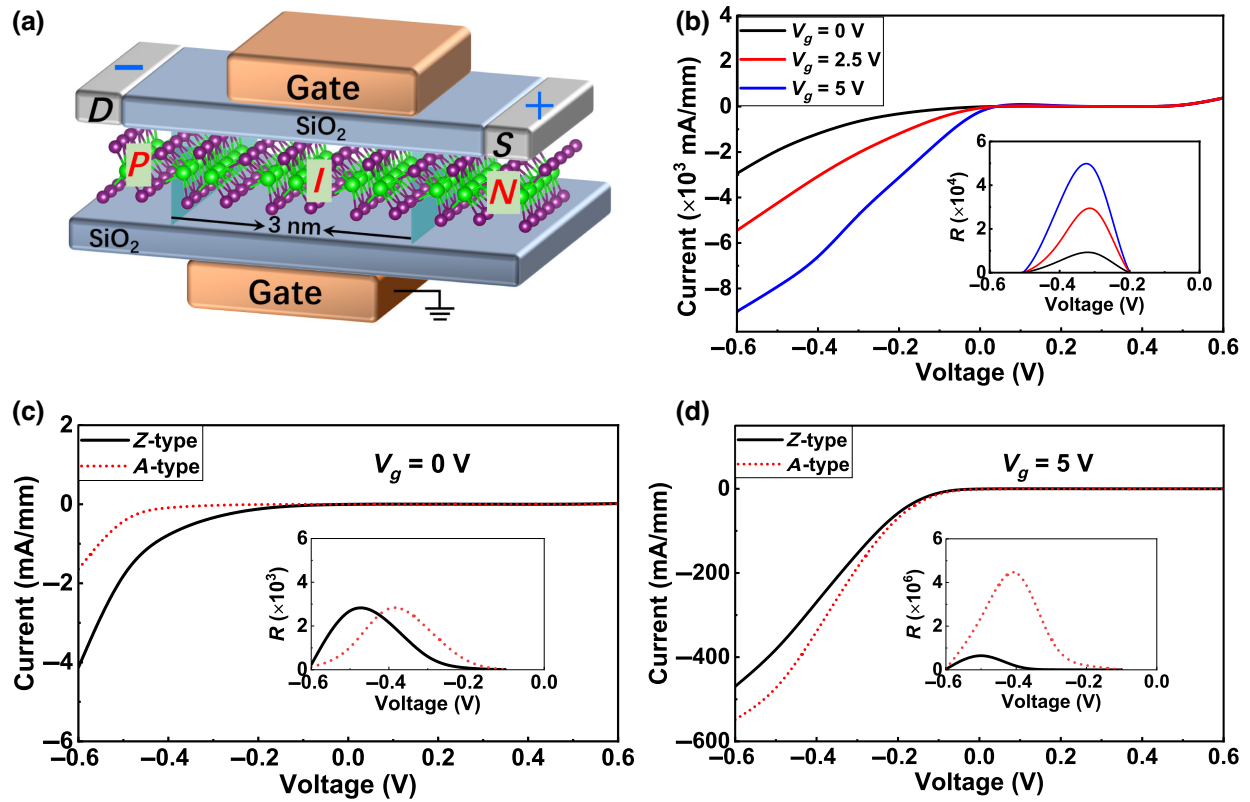


FIG. 7. Transport properties of the pin-junction FET of the 2D ZrI₂ monolayer. (a) Schematic of *p-i-n* junction FET. Bias-dependent current of (b) ml- α -phase *p-i-n* junction FET under gate voltages of 0, 2.5, and 5 V; and (c),(d) ml-*hex*-phase pin-junction FET under gate voltages of 0 and 5 V. The rectification ratio R is shown in the insets of (b)–(d).

1800 mA mm⁻¹ at 0.1 V on the positive-bias side. Then the current starts to decrease until it drops to almost zero at 0.3 V. This is because the transmission coefficient decreases with an increase in bias within a bias window of 0–0.3 V [see Fig. 6(c)]. Electrons can barely be transmitted when the positive bias is higher than 0.3 V because the transmission coefficients are almost zero in the bias region. On the negative-bias side, the current density reaches a maximum of approximately 14 000 mA mm⁻¹ at -0.45 V, and then decreases with increasing bias. This is attributed to the fact that the transmission performance decreases as the bias increases, as shown in the Figs. 6(b) and 6(e), that is, the transmission coefficient at -0.6 V bias is generally smaller than that at -0.5 bias. Furthermore, the k -dependent transmission coefficient $T(E, k)$ is calculated at a bias of -0.5 V, as shown in Fig. 6(f). The results reveal that the $T(E, k)$ remains high over the entire Brillouin zone around the Fermi level E_F .

For the *p-n* junction diode of the ml-*hex*-phase, the transport performance was investigated along the zigzag (x direction, denoted as Z type) and armchair (y direction, denoted as A type) directions of the lattice [see Fig. 1(b)] serving as the transmission directions. The I - V curves in

Fig. 5(c) show that the transmission current is generally smaller than that of the *p-n* junction diode of the ml- α -phase under the same bias. However, the unidirectional transport feature is significantly superior to the latter. The current is prohibited under a limited forward bias but is opened at the negative-bias side with a low threshold voltage of $V_{\text{on}} = -0.1$ V (A type) and -0.2 V (Z type). The current densities are approximately 2500 and 4500 mA mm⁻¹ at a bias of -0.5 V for the A type and Z type *p-n* junctions, respectively. In addition, the ml-*hex*-phase *p-n* junction demonstrates considerable electrical anisotropy. The maximum magnitudes of R for the A- and Z-type *p-n* junctions were 10⁷ and 10⁶, respectively, as shown in the left inset of Fig. 5(c). The R values are much larger than those of the graphene/*h*-BN heterojunction [85], VS₂/MoS₂ heterojunction [86], and CrSCl monolayer *p-n* junction [73], indicating the excellent unidirectional transport feature of the ml-*hex*-phase *p-n* junction. The transmission coefficient $T(E)$, PLDOS, transmission spectra $T(E, V)$, and k -dependent transmission coefficients $T(E, k)$ were also calculated, as shown in Fig. S6 within the Supplemental Material [75]. The A- and Z-type *p-n* junctions exhibit similar transport behaviors and rectifying mechanisms.

C. Field-effect properties of the ZrI₂ monolayer *p-i-n* junction transistor

Here, we constructed the *p-i-n* junction FETs with the ml- α -phase and ml-*hex*-phase of the ZrI₂ monolayer acting as the device channel, as shown in Fig. 7(a). The *p*- and *n*-doped ZrI₂ monolayers ($2.5 \times 10^{14} \text{ cm}^{-2}$) were used as electrodes on both sides of the FET, whereas the intrinsic monolayer was used in the central intrinsic region (i) as the device channel (approximately 3 nm). The introduction of a multigate scheme, with top and bottom gates placed near the central intrinsic region and covering the entire region, allows for the control of the vertical electric field applied to the device and further improves the transmission performance of the device. The current through the pin-junction FET is expressed as

$$I(V_b, V_g) = \frac{2e}{h} \int_{-\infty}^{\infty} T(E, V_b, V_g) [f_D(E - \mu_D) - f_S(E - \mu_S)] dE. \quad (7)$$

The *I-V* curves of the ml- α -phase *p-i-n* junction FET under gate voltages of 0, 2.5, and 5 V are shown in Fig. 7(b), while the *I-V* curves of the ml-*hex*-phase *p-i-n* junction FET under gate voltages of 0 and 5 V are shown in Figs. 7(c) and 7(d), respectively. Both the ml- α -phase and ml-*hex*-phase exhibit lower current density for the *p-i-n* junction FET under zero gate voltage compared to the *p-i-n* junction diode at the same bias owing to the semiconducting nature of the central intrinsic region. Furthermore, applying a gate voltage significantly enhances the current density, demonstrating excellent field-effect behavior. Moreover, for the ml- α -phase *p-i-n* junction FET, a current is generated when a negative bias is applied under various gate voltages. Nevertheless, the threshold bias voltage is approximately -0.4 and -0.2 V for the *A*- and *Z*-type ml-*hex*-phase *p-i-n* junction FET under zero gate voltage. Notably, a higher gate voltage can significantly reduce the threshold bias voltage, as evident from the comparison between Figs. 7(c) and 7(d). In addition, the rectification ratios *R* displayed in the insets of Figs. 7(b)–7(d) indicate that applying a higher gate voltage significantly improves the unidirectional transport feature of the FET. To further investigate the influence of the electric field in the opposite direction on the field-effect behavior of the *p-i-n* junction FET, we calculated the current density at a bias of -0.5 V under various gate voltages over a range of -5 to 5 V, as shown in Fig. S7 within the Supplemental Material [75]. For both ml- α -phase and ml-*hex*-phase *p-i-n* junction FETs, the effects of positive and negative gate voltages are symmetric. This is essentially determined by the symmetric structure and the existence of inversion center of the ml-*hex*-phase and ml- α -phase, respectively.

D. Optical and photoelectric properties of the ZrI₂ monolayer and its *p-i-n* junction phototransistor

To investigate the response of the ZrI₂ monolayer and the device to the optical spectrum, the optical properties and photoelectric performance were calculated using the Kubo-Greenwood approach [87] and DFT with the QuantumATK software, as shown in Fig. 8. We calculate the susceptibility tensor $\chi(\omega)$ according to the Kubo-Greenwood formula as [87]

$$\chi_{ij}(\omega) = -\frac{e^2 \hbar^4}{m^2 \varepsilon_0 V \omega^2} \sum_{nm} \frac{f(E_m) - f(E_n)}{E_{nm} - \hbar\omega - i\Gamma} \pi_{nm}^i \pi_{nm}^j, \quad (8)$$

where ω is an electromagnetic wave frequency, ε_0 is the dielectric constant, V is the volume, f is the Fermi-Dirac function, Γ is the broadening, and π_{nm}^i is the *i*th dipole matrix element between the states *n* and *m*. To better explain the optical response, electronic transitions from the first four valences below E_F to the first four conduction bands above E_F are considered. The optical conductivity, complex refractive index and absorption coefficient were calculated as [88]

$$\sigma = -i\omega\varepsilon_0\chi(\omega), n + ik = \sqrt{1 + i\frac{\sigma}{\varepsilon_0\omega}}, \alpha = 2\frac{\omega}{c}\kappa, \quad (9)$$

where $n(\omega)$ is the real refractive index, $\kappa(\omega)$ is the extinction coefficient, and c is the speed of light. The absorption coefficient and optical conductivity of the ml- α -phase ZrI₂ monolayer were calculated, as shown in Figs. 8(a) and 8(b), respectively. The absorption edge begins at an energy of approximately 0.4 eV, corresponding to an electronic band gap of 0.430 eV. The absorption coefficient curve has two main peaks at approximately 0.93 and 1.87 eV, and its maximum is at approximately $2.5 \times 10^5 \text{ cm}^{-1}$, comparable to that of the MoS₂ flake ($2.8 \times 10^6 \text{ cm}^{-1}$) [89]. The first absorption peak was in the infrared spectral region, while the second peak was in the red spectral region within the AM1.5 standard [90]. Figures 8(a) and 8(b) show the optical conductivity and the absorption spectrum. One can see that the positions of the optical conductivity peaks almost coincide with those of the absorption peaks. We constructed a phototransistor based on the *p-i-n* junction of the ZrI₂ monolayer, as shown in Fig. 8(g). For the ml- α -phase of the *p-i-n* junction phototransistor, the photocurrent is investigated using linearly polarized light as the optical excitation. The currents in the electrode of *D* or *S* excited by the absorption of photons with a frequency ω were calculated as [91,92]

$$I_\alpha = \frac{e}{h} \int_{-\infty}^{\infty} \sum_{\beta=D,S} [1 - f_\alpha(E)] f_\beta(E - \hbar\omega) T_{\alpha,\beta}^-(E) - f_\alpha(E) [1 - f_\beta(E + \hbar\omega)] T_{\alpha,\beta}^+(E) dE, \quad (10)$$

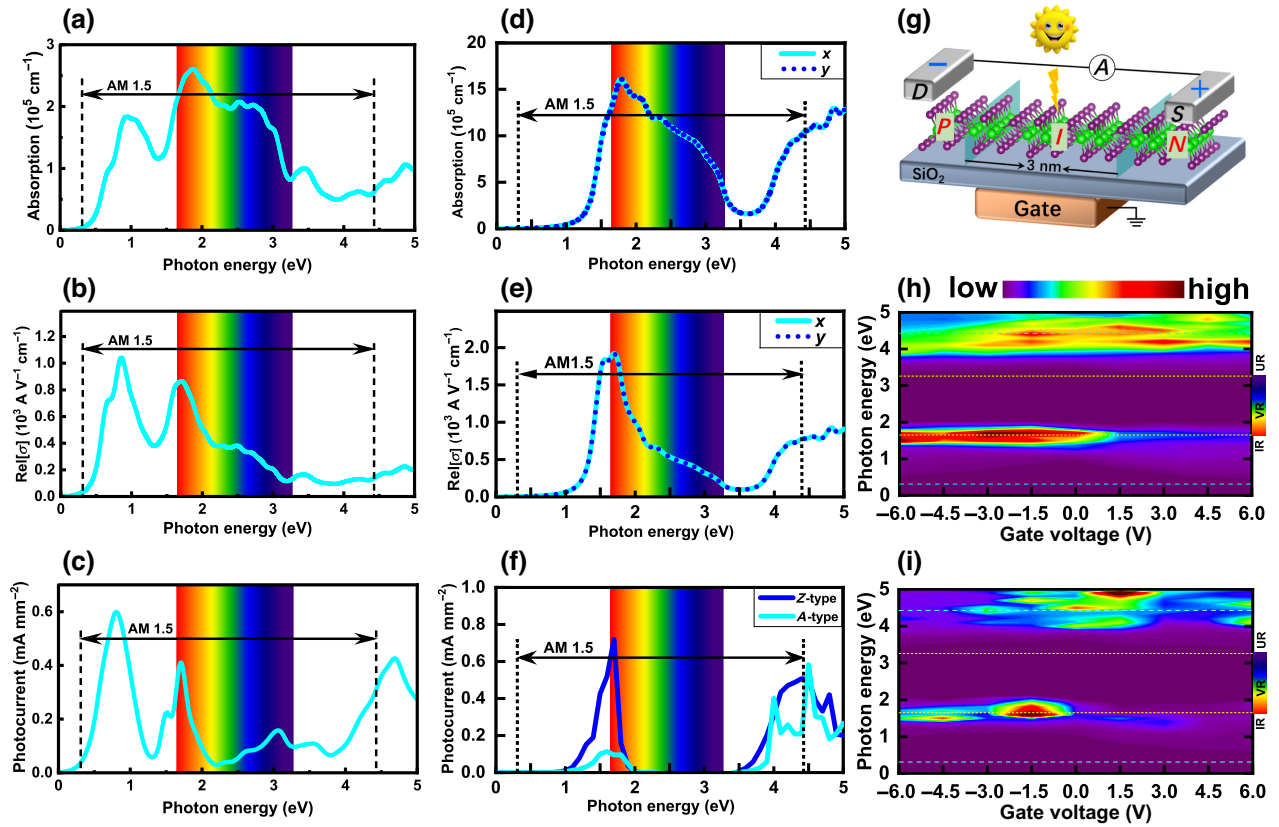


FIG. 8. (a) Optical absorption coefficient, (b) optical conductivity, and (c) photocurrent density of the ml- α -phase ZrI₂ monolayer. (d)–(f) The corresponding parameters of the ml-hex-phase ZrI₂ monolayer. (g) Schematic of the *p-i-n* junction phototransistor of the ZrI₂ monolayer. Gate-dependent photocurrent spectra of the ml-hex-phase *p-i-n* junction phototransistor along the zigzag (h) and armchair (i) directions. Embedded spectrum pattern in (a)–(f) displays visible-light region.

where $\alpha = D$ or S . The total photocurrent produced by the phototransistor was obtained as $I_{\text{ph}} = I_D - I_S$, as shown in Fig. 8(c). The photocurrent of the ml- α -phase *p-i-n* junction phototransistor has two large peaks in the infrared and red spectral region, corresponding to the peaks of the absorption coefficient and optical conductivity.

Furthermore, the optical performance of the ml-hex-phase ZrI₂ monolayer along the armchair and zigzag directions was calculated, as shown in Figs. 8(d)–8(f). Similar to other 2D materials [93,94], one can see that the absorption coefficient and optical conductivity of this phase are isotropic along the x and y directions, which is mainly due to the fact that the electronic bandstructure (around the Γ point) of the phase is isotropic in the Brillouin zone, as the 3D band and its 2D projections shown in Fig. 4(d). Both parameters exhibit one sharp peak in the red spectral region, corresponding to a photon energy of approximately 1.77 eV. Nevertheless, the ml-hex-phase *p-i-n* junction phototransistor exhibits anisotropic behavior [see Fig. 8(f)]. Although the positions of the photocurrent peaks along the two directions roughly coincide, the

heights of the peaks differ considerably, that is, the maximum photocurrent density along the zigzag direction is as high as 0.7 mA mm⁻², while that along the armchair direction is as low as 0.1 mA mm⁻². This difference may arise from the model error of the devices in different directions (e.g., the length of central region of zigzag and armchair devices are 3.0 and 3.3 nm, respectively). In addition, the gate-dependent photocurrent spectra of the ml-hex-phase *p-i-n* junction phototransistor along the zigzag and armchair directions were investigated, as shown in Figs. 8(h) and 8(i), respectively. One can see that the photocurrents of the ml-hex-phase *p-i-n* junction phototransistor are sensitive to electric fields. The negative gate voltage, especially in the -1.5 to -3 V region, can effectively enhance the photocurrent along the zigzag direction. The armchair direction exhibits strong selectivity to the gate voltage, with considerable enhancement of the photocurrent at a negative gate voltage of -1.5 V. These excellent optoelectronic characteristics and field-effect behaviors offer a broad range of possibilities for the practical application of such devices.

IV. SUMMARY

An extensive structural search of the bulk ZrI_2 was performed using first-principles total-energy calculations and the PSO algorithm. The experimentally synthesized monoclinic α - ZrI_2 phase ($P2_1/m$) was successfully reproduced, and three alternative structures with $P6_3/mmc$, $I4/mmm$, and $C2/m$ symmetries were predicted and identified. All phases exhibited a layered structure, and the calculated elastic constants and phonon dispersions confirmed their mechanic and dynamical stability. The cleavage energies of the ZrI_2 monolayer separated from the bulk α -, *hex*-, and *tet*-phases were estimated as 0.28, 0.23, and 0.37 J m⁻², respectively, indicating the feasibility of obtaining monolayer phases through mechanical exfoliation. The three ZrI_2 monolayers of the ml- α -phase, ml-*hex*-phase, and ml-*tet*-phase were mechanically and dynamically stable. The orientation-dependent Young's modulus, shear modulus, and Poisson's ratio for the monolayer ZrI_2 indicate that the ml- α -phase shows weak elastic anisotropy, the ml-*hex*-phase shows elastic isotropy, and the ml-*tet*-phase shows strong elastic anisotropy. Both the ml- α -phase and ml-*hex*-phase ZrI_2 monolayers are indirect band-gap semiconductors with band gap of 0.430 and 0.787 eV, respectively, whereas the ml-*tet*-phase is a metal and has a conelike band structure near the Fermi level similar to that of graphene.

Conceptual devices, such as *p-n* junction diodes, FETs, and phototransistors, were constructed using the ml- α -phase and ml-*hex*-phase of the ZrI_2 monolayer owing to their semiconducting character and high carrier mobility. The *I-V* curve of the *p-n* junction diode exhibited a strong NDC effect in a bias range of 0.1 to 0.4 V and -0.4 to -0.6 V for the ml- α -phase. The ml-*hex*-phase *p-n* junction diode demonstrated a low threshold voltage and high current density at the negative-bias side and exhibited excellent unidirectional transport feature. The transport performance of the *p-i-n* junction FET can be improved using a vertical electric field. The current densities of the devices were significantly enhanced when a gate voltage was applied. Furthermore, for the *A*- and *Z*-type ml-*hex*-phase *p-i-n* junction FET, a higher gate voltage significantly reduced the threshold bias voltage and improved unidirectional transport. The optical properties and photoresponse characteristics of the ZrI_2 monolayer phototransistor reveal sharp peaks in the infrared and red spectral regions for the optical absorption coefficient, optical conductivity, and photocurrent density, making them promising candidates for infrared and red photodetectors. Moreover, their sensitivity to gate voltages further expands their practical applications.

ACKNOWLEDGMENTS

We acknowledge funding from the National Natural Science Foundation of China (Grants No. 12274117, No.

62274066, and No. 62275074), the Natural Science Foundation of Henan Province (Grant No. 202300410226), the Young Top-notch Talents Project of Henan Province (2021 year), the Program for Innovative Research Team (in Science and Technology) in University of Henan Province (Grant No. 24IRTSTHN025), the Key Scientific Project of Universities of Henan Province (Grant No. 22A140020), and Henan Center for Outstanding Overseas Scientists (Grant No. GZS2023007). We thank the High Performance Computing Center of Henan Normal University.

-
- [1] A. C. Ferrari, F. Bonaccorso, V. Fal'ko, K. S. Novoselov, S. Roche, P. Bøggild, S. Borini, F. H. L. Koppens, V. Palermo, N. Pugno, *et al.*, Science and technology roadmap for graphene, related two-dimensional crystals, and hybrid systems, *Nanoscale* **7**, 4598 (2015).
 - [2] J. R. Schaibley, H. Yu, G. Clark, P. Rivera, J. S. Ross, K. L. Seyler, W. Yao, and X. Xu, Valleytronics in 2D materials, *Nat. Rev. Mater.* **1**, 16055 (2016).
 - [3] X. Wang, Y. Cui, T. Li, M. Lei, J. Li, and Z. Wei, Recent advances in the functional 2D photonic and optoelectronic devices, *Adv. Opt. Mater.* **7**, 1801274 (2019).
 - [4] T. Tan, X. Jiang, C. Wang, B. Yao, and H. Zhang, 2D material optoelectronics for information functional device applications: status and challenges, *Adv. Sci.* **7**, 2000058 (2020).
 - [5] E. C. Ahn, 2D materials for spintronic devices, *npj 2D Mater. Appl.* **4**, 17 (2020).
 - [6] A. Mogulkoc, Y. Mogulkoc, S. Jahangirov, and E. Durgun, Characterization and stability of Janus TiXY (X/Y = S, Se, and Te) monolayers, *J. Phys. Chem. C* **123**, 29922 (2019).
 - [7] P. Chen, Y. H. Chan, X. Y. Fang, Y. Zhang, M. Y. Chou, S. K. Mo, Z. Hussain, A. V. Fedorov, and T. C. Chiang, Charge density wave transition in single-layer titanium diselenide, *Nat. Commun.* **6**, 8943 (2015).
 - [8] B. Guster, E. Canadell, M. Pruneda, and P. Ordejón, First principles analysis of the CDW instability of single-layer 1T-TiSe₂ and its evolution with charge carrier density, *2D Mater.* **5**, 025024 (2018).
 - [9] S. İpek, M. E. Kilic, A. Mogulkoc, S. Cahangirov, and E. Durgun, Semiconducting defect-free polymorph of borophene: Peierls distortion in two dimensions, *Phys. Rev. B* **98**, 241408 (2018).
 - [10] H. Chen, J. Zhang, D. Kan, J. He, M. Song, J. Pang, S. Wei, and K. Chen, The recent progress of two-dimensional transition metal dichalcogenides and their phase transition, *Crystals* **12**, 1381 (2022).
 - [11] K. Jiang, T. Wu, J.-X. Yin, Z. Wang, M. Z. Hasan, S. D. Wilson, X. Chen, and J. Hu, Kagome superconductors AV₃Sb₅ (A = K, Rb, Cs), *Natl. Sci. Rev.* **10**, nwac199 (2023).
 - [12] M.-Y. Li, S.-K. Su, H.-S. P. Wong, and L.-J. Li, How 2D semiconductors could extend Moore's law, *Nature* **567**, 169 (2019).
 - [13] H. Liu, A. T. Neal, Z. Zhu, Z. Luo, X. Xu, D. Tománek, and P. D. Ye, Phosphorene: An unexplored 2D semiconductor with a high hole mobility, *ACS Nano* **8**, 4033 (2014).

- [14] L. Kou, C. Chen, and S. C. Smith, Phosphorene: Fabrication, properties, and applications, *J. Phys. Chem. Lett.* **6**, 2794 (2015).
- [15] A. Carvalho, M. Wang, X. Zhu, A. S. Rodin, H. Su, and A. H. Castro Neto, Phosphorene: From theory to applications, *Nat. Rev. Mater.* **1**, 16061 (2016).
- [16] M. Batmunkh, M. Bat-Erdene, and J. G. Shapter, Phosphorene and phosphorene-based materials – prospects for future applications, *Adv. Mater.* **28**, 8586 (2016).
- [17] M. Zhang, G. M. Biesold, and Z. Lin, A multifunctional 2D black phosphorene-based platform for improved photovoltaics, *Chem. Soc. Rev.* **50**, 13346 (2021).
- [18] J. Guan, A. M. Rao, J. Zhou, X. Yu, and B. Lu, Structure-optimized phosphorene for super-stable potassium storage, *Adv. Funct. Mater.* **32**, 2203522 (2022).
- [19] B. Anasori, M. R. Lukatskaya, and Y. Gogotsi, 2D metal carbides and nitrides (MXenes) for energy storage, *Nat. Rev. Mater.* **2**, 16098 (2017).
- [20] Y. Gogotsi and B. Anasori, The rise of MXenes, *ACS Nano* **13**, 8491 (2019).
- [21] M. Chhowalla, H. S. Shin, G. Eda, L.-J. Li, K. P. Loh, and H. Zhang, The chemistry of two-dimensional layered transition metal dichalcogenide nanosheets, *Nat. Chem.* **5**, 263 (2013).
- [22] Q. H. Wang, K. Kalantar-Zadeh, A. Kis, J. N. Coleman, and M. S. Strano, Measurement of mobility in dual-gated MoS₂ transistors, *Nat. Nanotechnol.* **7**, 699 (2012).
- [23] Y. An, M. Zhang, D. Wu, Z. Fu, and K. Wang, The electronic transport properties of transition-metal dichalcogenide lateral heterojunctions, *J. Mater. Chem. C* **4**, 10962 (2016).
- [24] S. Manzeli, D. Ovchinnikov, D. Pasquier, O. V. Yazyev, and A. Kis, 2D transition metal dichalcogenides, *Nat. Rev. Mater.* **2**, 17033 (2017).
- [25] T. Chowdhury, E. C. Sadler, and T. J. Kempa, Progress and prospects in transition-metal dichalcogenide research beyond 2D, *Chem. Rev.* **120**, 12563 (2020).
- [26] E. C. Regan, D. Wang, E. Y. Paik, Y. Zeng, L. Zhang, J. Zhu, A. H. MacDonald, H. Deng, and F. Wang, Emerging exciton physics in transition metal dichalcogenide heterobilayers, *Nat. Rev. Mater.* **7**, 778 (2022).
- [27] K. S. Novoselov, A. K. Geim, S. V. Morozov, D. Jiang, Y. Zhang, S. V. Dubonos, I. V. Grigorieva, and A. A. Firsov, Electric field effect in atomically thin carbon films, *Science* **306**, 666 (2004).
- [28] H. Suzuki, N. Ogura, T. Kaneko, and T. Kato, Highly stable persistent photoconductivity with suspended graphene nanoribbons, *Sci. Rep.* **8**, 11819 (2018).
- [29] Z. Yu, Z.-Y. Ong, Y. Pan, Y. Cui, R. Xin, Y. Shi, B. Wang, Y. Wu, T. Chen, Y.-W. Zhang, *et al.*, Realization of room-temperature phonon-limited carrier transport in monolayer MoS₂ by dielectric and carrier screening, *Adv. Mater.* **28**, 547 (2016).
- [30] Y. Wang, J. C. Kim, R. J. Wu, J. Martinez, X. Song, J. Yang, F. Zhao, A. Mkhoyan, H. Y. Jeong, *et al.*, Van der Waals contacts between three-dimensional metals and two-dimensional semiconductors, *Nature* **568**, 70 (2019).
- [31] C. Chen, M. Wang, J. Wu, H. Fu, H. Yang, Z. Tian, T. Tu, H. Peng, Y. Sun, X. Xu, *et al.*, Electronic structures and unusually robust bandgap in an ultrahigh-mobility layered oxide semiconductor, Bi₂O₂Se, *Sci. Adv.* **4**, eaat8355 (2018).
- [32] V. V. Kulish and W. Huang, Single-layer metal halides MX₂ (X = Cl, Br, I): stability and tunable magnetism from first principles and Monte Carlo simulations, *J. Mater. Chem. C* **5**, 8734 (2017).
- [33] R. E. Brandt, R. C. Kurchin, R. L. Z. Hoye, J. R. Poindexter, M. W. B. Wilson, S. Sulekar, F. Lenahan, P. X. T. Yen, V. Stevanović, J. C. Nino, *et al.*, Investigation of bismuth triiodide (BiI₃) for photovoltaic applications, *J. Phys. Chem. Lett.* **6**, 4297 (2015).
- [34] F. Ma, M. Zhou, Y. Jiao, G. Gao, Y. Gu, A. Bilic, Z. Chen, and A. Du, Single layer bismuth iodide: Computational exploration of structural, electrical, mechanical and optical properties, *Sci. Rep.* **5**, 17558 (2015).
- [35] H. Liu, X. Wang, J. Wu, Y. Chen, J. Wan, R. Wen, J. Yang, Y. Liu, Z. Song, and L. Xie, Vapor deposition of magnetic van der Waals NiI₂ crystals, *ACS Nano* **14**, 10544 (2020).
- [36] Y. An, H. Wang, J. Liao, Y. Gao, J. Chen, Y. Wu, Y. Li, G. Xu, and C. Ma, Spin transport properties and nanodevice simulations of NiI₂ monolayer, *Phys. E (Amsterdam, Neth.)* **142**, 115262 (2022).
- [37] X. Huang, L. Yan, Y. Zhou, Y. Wang, H.-Z. Song, and L. Zhou, Group 11 transition-metal halide monolayers: High promises for photocatalysis and quantum cutting, *J. Phys. Chem. Lett.* **12**, 525 (2021).
- [38] A. S. Toulouse, B. P. Isaacoff, G. Shi, M. Matuchová, E. Kioupakis, and R. Merlin, Frenkel-like Wannier-Mott excitons in few-layer PbI₂, *Phys. Rev. B* **91**, 165308 (2015).
- [39] M. Zhou, W. Duan, Y. Chen, and A. Du, Single layer lead iodide: computational exploration of structural, electronic and optical properties, strain induced band modulation and the role of spin-orbital-coupling, *Nanoscale* **7**, 15168 (2015).
- [40] M. Zhong, S. Zhang, L. Huang, J. You, Z. Wei, X. Liu, and J. Li, Large-scale 2D PbI₂ monolayers: experimental realization and their indirect band-gap related properties, *Nanoscale* **9**, 3736 (2017).
- [41] T. Zhang, Y. Liang, X. Xu, B. Huang, Y. Dai, and Y. Ma, Ferroelastic-ferroelectric multiferroics in a bilayer lattice, *Phys. Rev. B* **103**, 165420 (2021).
- [42] N. Ding, J. Chen, C. Gui, H. You, X. Yao, and S. Dong, Phase competition and negative piezoelectricity in interlayer-sliding ferroelectric ZrI₂, *Phys. Rev. Mater.* **5**, 084405 (2021).
- [43] X. Ma, C. Liu, W. Ren, and S. A. Nikolaev, Tunable vertical ferroelectricity and domain walls by interlayer sliding in β -ZrI₂, *npj Comput. Mater.* **7**, 177 (2021).
- [44] J. Zhou, Photo-magnetization in two-dimensional sliding ferroelectrics, *npj 2D Mater. Appl.* **6**, 15 (2022).
- [45] B. Luo, X. Ma, J. Liu, W. Wu, X. Yu, S. Hu, H. Gao, F. Jia, and W. Ren, Enhanced photogalvanic effect in a 2D ferroelectric ZrI₂ by interlayer sliding, *Phys. E (Amsterdam, Neth.)* **142**, 115297 (2022).
- [46] M. Jia, C.-L. Yang, M.-S. Wang, and X.-G. Ma, High dimensionless figure of merit of the ZrI₂ monolayer identified based on intrinsic carrier concentration and bipolar effect, *Appl. Phys. Lett.* **121**, 123903 (2022).
- [47] J. Wen, J. Peng, B. Zhang, and Z.-Y. Wang, Theoretical determination of superior high-temperature thermoelectricity

- in an n-type doped 2H-ZrI₂ monolayer, *Nanoscale* **15**, 4397 (2023).
- [48] J. Guo, Z. Lu, K. Wang, X. Zhao, G. Hu, X. Yuan, and J. Ren, Large valley polarization in a novel two-dimensional semiconductor H-ZrX₂ (X = Cl, Br, I), *J. Phys.: Condens. Matter* **34**, 075701 (2022).
- [49] C. Zhang, R. Wang, H. Mishra, and Y. Liu, Two-dimensional semiconductors with high intrinsic carrier mobility at room temperature, *Phys. Rev. Lett.* **130**, 087001 (2023).
- [50] D. H. Guthrie and J. D. Corbett, Synthesis and structure of an infinite-chain form of ZrI₂ (α), *J. Solid State Chem.* **37**, 256 (1981).
- [51] J. D. Corbett and D. H. Guthrie, A second infinite-chain form of zirconium diiodide (.beta.) and its coherent intergrowth with .alpha.-zirconium diiodide, *Inorg. Chem.* **21**, 1747 (1982).
- [52] R. Zacharia, H. Ulbricht, and T. Hertel, Interlayer cohesive energy of graphite from thermal desorption of polyaromatic hydrocarbons, *Phys. Rev. B* **69**, 155406 (2004).
- [53] Computational 2D Materials Database: <https://cmrdb.fysik.dtu.dk/c2db/row/ZrI2-9c024b5a2e89>
- [54] Y. Wang, J. Lv, L. Zhu, and Y. Ma, Crystal structure prediction via particle-swarm optimization, *Phys. Rev. B* **82**, 094116 (2010).
- [55] M. Brandbyge, J.-L. Mozos, P. Ordejón, J. Taylor, and K. Stokbro, Density-functional method for nonequilibrium electron transport, *Phys. Rev. B* **65**, 165401 (2002).
- [56] G. Kresse and J. Furthmüller, Efficient iterative schemes for *ab initio* total-energy calculations using a plane-wave basis set, *Phys. Rev. B* **54**, 11169 (1996).
- [57] G. Kresse and J. Furthmüller, Efficiency of *ab-initio* total energy calculations for metals and semiconductors using a plane-wave basis set, *Comput. Mater. Sci.* **6**, 15 (1996).
- [58] P. E. Blöchl, Projector augmented-wave method, *Phys. Rev. B* **50**, 17953 (1994).
- [59] G. Kresse and D. Joubert, From ultrasoft pseudopotentials to the projector augmented-wave method, *Phys. Rev. B* **59**, 1758 (1999).
- [60] J. P. Perdew, K. Burke, and M. Ernzerhof, Generalized gradient approximation made simple, *Phys. Rev. Lett.* **77**, 3865 (1996).
- [61] Y. Wang, J. Lv, L. Zhu, and Y. Ma, CALYPSO: A method for crystal structure prediction, *Comput. Phys. Commun.* **183**, 2063 (2012).
- [62] P. Gao, B. Gao, S. Lu, H. Liu, J. Lv, Y. Wang, and Y. Ma, Structure search of two-dimensional systems using CALYPSO methodology, *Front. Phys.* **17**, 23203 (2021).
- [63] Y. Wang, J. Lv, P. Gao, and Y. Ma, Crystal structure prediction via efficient sampling of the potential energy surface, *Acc. Chem. Res.* **55**, 2068 (2022).
- [64] J. Lv, Y. Wang, L. Zhu, and Y. Ma, Predicted novel high-pressure phases of lithium, *Phys. Rev. Lett.* **106**, 015503 (2011).
- [65] Y. Guo, C. Wang, W. Qiu, X. Ke, P. Huai, C. Cheng, Z. Zhu, and C. Chen, Structural and electronic phase transitions of ThS₂ from first-principles calculations, *Phys. Rev. B* **94**, 134104 (2016).
- [66] M. Xu, C. Huang, Y. Li, S. Liu, X. Zhong, P. Jena, E. Kan, and Y. Wang, Electrical control of magnetic phase transition in a type-I multiferroic double-metal trihalide monolayer, *Phys. Rev. Lett.* **124**, 067602 (2020).
- [67] X. Wang, Z. Wang, P. Gao, C. Zhang, J. Lv, H. Wang, H. Liu, Y. Wang, and Y. Ma, Data-driven prediction of complex crystal structures of dense lithium, *Nat. Commun.* **14**, 2924 (2023).
- [68] X. Hu, R.-W. Zhang, D.-S. Ma, Z. Cai, D. Geng, Z. Sun, Q. Zhao, J. Gao, P. Cheng, L. Chen, *et al.*, Realization of a Two-dimensional checkerboard lattice in monolayer Cu₂N, *Nano Lett.* **23**, 5610 (2023).
- [69] S. Grimme, J. Antony, S. Ehrlich, and H. Krieg, A consistent and accurate *ab initio* parametrization of density functional dispersion correction (DFT-D) for the 94 elements H-Pu, *J. Chem. Phys.* **132**, 154104 (2010).
- [70] S. Grimme, S. Ehrlich, and L. Goerigk, Effect of the damping function in dispersion corrected density functional theory, *J. Comput. Chem.* **32**, 1456 (2011).
- [71] S. Smidstrup, T. Markussen, P. Vancaerfeld, J. Wellendorf, J. Schneider, T. Gunst, B. Verstichel, D. Stradi, P. A. Khomyakov, U. G. Vej-Hansen, *et al.*, QuantumATK: An integrated platform of electronic and atomistic-scale modelling tools, *J. Phys.: Condens. Matter* **32**, 015901 (2020).
- [72] M. J. van Setten, M. Giantomassi, E. Bousquet, M. J. Verstraete, D. R. Hamann, X. Gonze, and G. M. Rignanese, The PseudoDojo: Training and grading a 85 element optimized norm-conserving pseudopotential table, *Comput. Phys. Commun.* **226**, 39 (2018).
- [73] J. Chen, Y. Guo, C. Ma, S. Gong, C. Zhao, T. Wang, X. Dong, Z. Jiao, S. Ma, G. Xu, *et al.*, Magnetic nanodevices and spin-transport properties of a two-dimensional CrScI monolayer, *Phys. Rev. Appl.* **19**, 054013 (2023).
- [74] H. J. Monkhorst and J. D. Pack, Special points for Brillouin-zone integrations, *Phys. Rev. B* **13**, 5188 (1976).
- [75] See the Supplemental Material at <http://link.aps.org/supplemental/10.1103/PhysRevApplied.20.064048> for Figs. S1–S7, Table S1, and the mechanical stability criteria for the bulk phases of ZrI₂, which includes Refs. [50,51,77,78].
- [76] X. Huang, Z. Zhuo, L. Yan, Y. Wang, N. Xu, H.-Z. Song, and L. Zhou, Single-layer zirconium dihalides ZrX₂ (X = Cl, Br, and I) with abnormal ferroelastic behavior and strong anisotropic light absorption ability, *J. Phys. Chem. Lett.* **12**, 7726 (2021).
- [77] M. Born and K. Huang, *Dynamic Theory of Crystal Lattice* (Oxford University Press, Oxford, 1954).
- [78] F. Mouhat and F.-X. Coudert, Necessary and sufficient elastic stability conditions in various crystal systems, *Phys. Rev. B* **90**, 224104 (2014).
- [79] Y. Le Page and P. Saxe, Symmetry-general least-squares extraction of elastic data for strained materials from *ab initio* calculations of stress, *Phys. Rev. B* **65**, 104104 (2002).
- [80] V. Wang, G. Tang, Y.-C. Liu, R.-T. Wang, H. Mizuseki, Y. Kawazoe, J. Nara, and W. T. Geng, High-throughput computational screening of two-dimensional semiconductors, *J. Phys. Chem. Lett.* **13**, 11581 (2022).
- [81] C. Jasiukiewicz, T. Paszkiewicz, and S. Wolski, Auxetic properties and anisotropy of elastic material constants of 2D crystalline media, *Phys. Status Solidi B* **245**, 562 (2008).

- [82] C. Jasiukiewicz, T. Paszkiewicz, and S. Wolski, Auxetic properties and anisotropy of elastic material constants of 2D crystalline media [Phys. Status Solidi B **245**, No. 3, 562–569 (2008)], [Phys. Status Solidi B **247**, 1247 \(2010\)](#).
- [83] D. Stradi, U. Martinez, A. Blom, M. Brandbyge, and K. Stokbro, General atomistic approach for modeling metal-semiconductor interfaces using density functional theory and nonequilibrium Green's function, [Phys. Rev. B **93**, 155302 \(2016\)](#).
- [84] M. Büttiker, Y. Imry, R. Landauer, and S. Pinhas, Generalized many-channel conductance formula with application to small rings, [Phys. Rev. B **31**, 6207 \(1985\)](#).
- [85] Y. An, M. Zhang, D. Wu, T. Wang, Z. Jiao, C. Xia, Z. Fu, and K. Wang, The rectifying and negative differential resistance effects in graphene/h-BN nanoribbon heterojunctions, [Phys. Chem. Chem. Phys. **18**, 27976 \(2016\)](#).
- [86] Y. An, Y. Hou, K. Wang, S. Gong, C. Ma, C. Zhao, T. Wang, Z. Jiao, H. Wang, and R. Wu, Multifunctional lateral transition-metal disulfides heterojunctions, [Adv. Funct. Mater. **30**, 2002939 \(2020\)](#).
- [87] J. E. Sipe and E. Ghahramani, Nonlinear optical response of semiconductors in the independent-particle approximation, [Phys. Rev. B **48**, 11705 \(1993\)](#).
- [88] R. M. Martin, *Electronic Structure: Basic Theory and Practical Methods* (Cambridge University Press, Cambridge, 2020).
- [89] J. Y. Kwak, Absorption coefficient estimation of thin MoS₂ film using attenuation of silicon substrate Raman signal, [Results Phys. **13**, 102202 \(2019\)](#).
- [90] G. ASTM, 173-03, *Terrestrial Reference Spectra for Photovoltaic Performance Evaluation* (American Society for Testing Materials (ASTM) International, West Conshohocken, 2012).
- [91] M. Palsgaard, T. Markussen, T. Gunst, M. Brandbyge, and K. Stokbro, Efficient first-principles calculation of phonon-assisted photocurrent in large-scale solar-cell devices, [Phys. Rev. Appl. **10**, 014026 \(2018\)](#).
- [92] L. Zhang, K. Gong, J. Chen, L. Liu, Y. Zhu, D. Xiao, and H. Guo, Generation and transport of valley-polarized current in transition-metal dichalcogenides, [Phys. Rev. B **90**, 195428 \(2014\)](#).
- [93] Y. Gao, J. Liao, H. Wang, Y. Wu, Y. Li, K. Wang, C. Ma, S. Gong, T. Wang, X. Dong, *et al.*, Electronic transport properties and nanodevice designs for monolayer MoSi₂P₄, [Phys. Rev. Appl. **18**, 034033 \(2022\)](#).
- [94] S. A. Yamusa, A. Shaari, N. A. M. Alsaif, I. M. Alsalamah, I. Isah, and N. Rekik, Elucidating the structural, electronic, elastic, and optical properties of bulk and monolayer MoS₂ transition-metal dichalcogenides: A DFT approach, [ACS Omega **7**, 45719 \(2022\)](#).